

First search for r-mode gravitational waves from PSR J0537-6910

LIUDMILA FESIK^{1,2} AND MARIA ALESSANDRA PAPA^{1,2,3}

¹Max Planck Institute for Gravitational Physics (Albert Einstein Institute), Callinstrasse 38, 30167 Hannover, Germany

²Leibniz Universität Hannover, D-30167 Hannover, Germany

³University of Wisconsin Milwaukee, 3135 N Maryland Ave, Milwaukee, WI 53211, USA

ABSTRACT

We report results of the first search to date for continuous gravitational waves from unstable r-modes from the pulsar PSR J0537-6910. We use data from the first two observing runs of the Advanced LIGO network. We find no significant signal candidate and set upper limits on the amplitude of gravitational-wave signals, which are within an order of magnitude of the spin-down values. We highlight the importance of having timing information at the time of the gravitational-wave observations, i.e. rotation frequency and frequency-derivative values, and glitch-occurrence times, such as those that a NICER (NICER 2017) campaign could provide.

Keywords: gravitational waves, neutron stars, pulsars

1. INTRODUCTION

Fast-spinning neutron stars are among the most promising sources of gravitational radiation. Non-axisymmetric deformations and “wobbles” of rotating stars will produce quasi-monochromatic long-lasting gravitational emission – continuous gravitational waves (CWs). In addition, gravitational radiation can destabilize *r-modes* – quasi-normal stellar oscillations of rotating stars (Andersson 1998; Friedman & Morsink 1998; Owen et al. 1998) – and give rise to substantial continuous gravitational-wave emission. This instability is particularly interesting in hot young neutron stars because it could provide an effective spin-down mechanism (Lindblom et al. 1998).

If neutron stars form in collapse processes, from the conservation of angular momentum one might expect their initial spin to be close to the theoretical maximum that their structure could support, between 500 and 2000 Hz, depending on the equation of state. The observations, however, indicate that young neutron stars present rather smaller spins. Gravitational-wave driven r-mode instabilities have been put forward as a mechanism to explain the missing young fast-rotating pulsars

(Andersson et al. 1999) and concrete detection strategies have been proposed (Owen 2010; Caride et al. 2019).

The fastest and the most energetic known young pulsar is PSR J0537-6910. This object is associated with the supernova remnant N157B in the Large Magellanic Cloud, its age is estimated to be 4000 yr, and it is spinning at about 62 Hz (Marshall et al. 1998; Townsley et al. 2006). This spin frequency may be just below the predicted final frequency for the r-mode emission mechanism (Alford & Schwenzer 2014, 2015).

The analysis of 13 years (1999–2011) of X-ray spin timing observations of PSR J0537-6910 with the Rossi X-ray Timing Explorer (RXTE) has revealed an extreme glitch activity with abrupt spin-ups (*glitches*) every few months and a subsequent post-glitch relaxation phase (Antonopoulou et al. 2018). A recent study of the post-relaxation phase data has found an intriguing indication: the average braking index during these periods is ≈ 7.4 (Andersson et al. 2018).

Why is this intriguing? The braking index n is commonly used to describe the spin evolution of neutron stars, $\dot{\nu}(t) \propto \nu(t)^n$, with $n = \nu\ddot{\nu}/\dot{\nu}^2$, with ν indicating the spin frequency. If the star’s spin evolution is driven by magnetic dipole emission $n = 3$; if quadrupolar gravitational-wave emission is the culprit then $n = 5$; for r-modes $n = 7$, under some approximations (Kokkotas & Schwenzer 2016; Alford & Schwenzer 2014). This means that the measured value of the braking index $n \sim 7.4$ might suggest that unstable r-mode emission

liudmila.fesik@aei.mpg.de

maria.alessandra.papa@aei.mpg.de

is the main driver of the spin evolution of PSR J0537-6910.

With this background we perform a directed search for continuous gravitational waves from PSR J0537-6910 assuming that the emission stems from unstable r-modes. We use data from the Advanced LIGO network (aLIGO) (Vallisneri et al. 2015; LIGO 2018a,b) spanning the period between Sept, 2015 and Aug, 2017. Since electromagnetic (EM) observations of J0537 are not available for this period, the pulsar’s rotational parameters are not precisely known and its glitch activity is unknown.

The paper is organized as follows. We summarise relevant results from the timing analysis of EM data in Sec. 2. Relations between the expected gravitational-wave frequency and the spin of the pulsar are defined in Sec. 3 and the search is detailed in Sec. 4. Results are presented in Sec. 5 and discussed in Sec. 6.

2. SPIN EVOLUTION OF J0537-6910

PSR J0537-6910 is spinning at ≈ 62 Hz with a strong spin-down rate $\dot{\nu} \approx -2 \times 10^{-10}$ Hz/s. Its spin evolution is usually described as the superposition of two trends: the long-term (LT) evolution that describes the spin evolution on the timescale of years and the short-term (ST) evolution that describes the post-glitch recovery phase and is appropriate for weeks after a glitch (Antonopoulou et al. 2018).

The long-term braking index n_{LT} of J0537-6910 is derived by fitting the measurements of $\dot{\nu}$ at the mid-time epochs between two subsequent glitches over 13 years of data. The result is $n_{LT} = -1.22$ with a negative second-order frequency derivative $\ddot{\nu}_{LT} = -7.7 \times 10^{-22}$ Hz/s² (Antonopoulou et al. 2018).

We will refer to the periods between two successive glitches as glitch-free or inter-glitch intervals. The inter-glitch spin evolution is estimated through a phase-coherent timing analysis of the 45 known inter-glitch intervals and yields a wide range of braking indices, with most $n_{ig} > 10$ (Antonopoulou et al. 2018). A detailed analysis (Andersson et al. 2018) shows that the largest contributions to n_{ig} come from epochs ≤ 50 days after a glitch, indicating the existence of an early fast relaxation phase. In contrast, an asymptotic value of n_{ig} for the longer time intervals is ≈ 7.4 (Fig. 3 in (Andersson et al. 2018)), which might reflect the fact that gravitational-wave emission due to r-mode instability is causing the observed spin down. Incorporating the effect of temperature and frequency on the saturation amplitude yields values of the braking index different from ~ 7 (Kokkotas & Schwenzer 2016; Alford & Schwenzer 2014). In this search we assume a constant value of the braking in-

dex derived from the timing analyses and neglect these effects. For simplicity we will assume that r-mode emission sets in 50 days after a glitch.

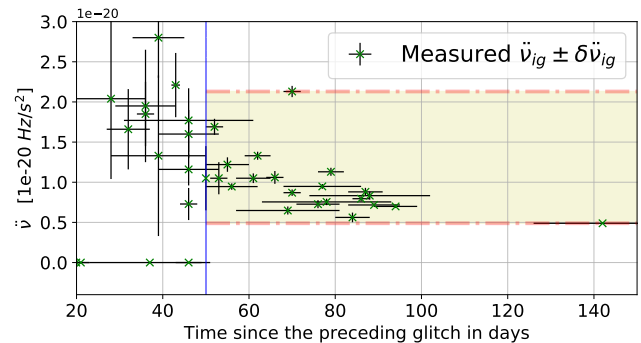


Figure 1. Distribution of measured $\ddot{\nu}_{ig} \pm \delta\ddot{\nu}_{ig}$ for every known inter-glitch period, as a function of the fit epoch. The fit epoch is 0 at the time of each glitch. (We used the data from Tab. 1 of (Antonopoulou et al. 2018).)

Table 1. Sky position and spin evolution parameters for PSR J0537-6910 (Townsend et al. 2006; Antonopoulou et al. 2018)

Sky position			
α [deg]	84.4476	δ [deg]	-69.17219
Long-term evolution			
n_{LT}	-1.22 ± 0.04	$\ddot{\nu}_{LT}$ [Hz/s ²]	$-7.7 \times 10^{-22} \pm 3 \times 10^{-23}$
Short-term evolution			
n_{ig}	7.4 ± 0.7	$\ddot{\nu}_{ig}^{\min}$ [Hz/s ²]	$4.89 \times 10^{-21} \pm 7 \times 10^{-23}$
		$\ddot{\nu}_{ig}^{\max}$ [Hz/s ²]	$2.13 \times 10^{-20} \pm 7 \times 10^{-22}$
The last observation			
fit epoch t_{obs} [GPS]	1004659215		
$\nu _{t_{obs}}$ [Hz]	$61.961105096 \pm 5 \times 10^{-9}$		

Fig. 1 shows the second-order frequency-derivative values for the various inter-glitch periods as a function of the epoch of the measurement. For epochs that more than 50 days after the glitch, $\ddot{\nu}_{ig} \in [4.89(7) \times 10^{-21}, 2.13(7) \times 10^{-20}]$ Hz/s², as shown in Tab. 1 of (Antonopoulou et al. 2018).

The most important values from the timing analysis of PSR J0537-6910 are summarized in Tab. 1.

3. GRAVITATIONAL-WAVE EMISSION FROM R-MODES

The strongest gravitational waves are expected from the quadrupole ($l = m = 2$) r-mode, so we concentrate on this. The gravitational-wave frequency f associated with this mode depends on the neutron star structure and its rotation frequency ν in a non-trivial manner (Owen et al. 1998; Lindblom et al. 1998). We follow the prescription of (Caride et al. 2019) and use the following relations:

$$\begin{cases} f/\nu = A - B(\nu/\nu_K)^2 \\ \dot{f}/\dot{\nu} = A - 3B(\nu/\nu_K)^2 \\ \ddot{f}/\ddot{\nu} = A - 3B(\nu/\nu_K)^2(1 - \frac{2}{n}) \end{cases} \quad (1)$$

with n being the braking index during the r-mode phase, ν_K the Kepler frequency of the star, and the quantities $1.39 \leq A \leq 1.57$ and $0 \leq B \leq 0.195$ encoding information on the neutron star structure. Based on the observed highest spin frequency of pulsars at 716 Hz, following (Caride et al. 2019), we take 506 Hz as a lower bound for ν_K . Using this value yields a broader (i.e. more conservative) search range than for a ν_K in line with the standard estimates for neutron stars and higher by a factor of 2 or 3 (Glendenning 1992; Paschalidis & Stergioulas 2017).

The uncertainties in the values of A and B give rise to ranges of values for the gravitational-wave frequency and frequency derivatives. Since A is always $\gg 3B(\nu/\nu_K)^2$ they take the form

$$\begin{cases} \left(1.39 - 0.195 \frac{\nu^2}{\nu_K^2}\right) \nu \leq f \leq 1.57 \nu \\ \left(1.39 - 0.585 \frac{\nu^2}{\nu_K^2}\right) |\dot{\nu}| \leq |\dot{f}| \leq 1.57 |\dot{\nu}| \\ \left(1.39 - 0.585 \frac{\nu^2}{\nu_K^2}\right) \left(1 - \frac{2}{n}\right) \ddot{\nu} \leq \ddot{f} \leq 1.57 \ddot{\nu} \end{cases} \quad (2)$$

and we note that $\dot{\nu} = -|\dot{\nu}|$ and $\dot{f} = -|\dot{f}|$.

4. THE GRAVITATIONAL-WAVE SEARCH

4.1. The data input

We use the data from the two Advanced LIGO (aLIGO) detectors located in Hanford (WA) and Livingston (LA), USA (Abbott et al. 2009). We search the publicly available data from the first two observing runs O1 and O2 (LIGO 2018a,b; Vallisneri et al. 2015). O1 took place between September 12, 2015 and January 19, 2016 and covered about 4 months of data (Abbott et al. 2016; Aasi et al. 2015). The second run (O2) operated from 2016 November 30 to 2017 August 25 and includes

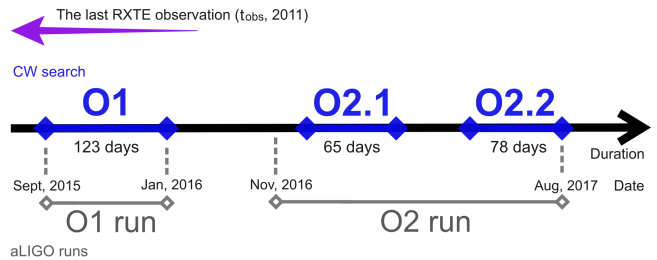


Figure 2. The data from the O1 and O2 aLIGO observing runs used for our searches.

a significant gap in the data between 2017 March 15th and June 8th (Abbott et al. 2019b; LIGO 2018c). This gap naturally provides two stretches of contiguous data, which we consider as two independent time baselines for our searches: *O2.1* and *O2.2*, as shown in Fig. 2.

The search input consists of short time baseline Fourier transforms (SFTs) (Allen & Mendell 2004), from data segments 1800s long. Instrumental and environmental spectral disturbances are removed to avoid contamination of the results, as done in previous searches (Covas et al. 2018; Abbott et al. 2017).

4.2. The signal waveform

The signal at each detector, $h(t)$, is a superposition of the two polarization waveforms $h_+(t)$ and $h_\times(t)$

$$h(t) = F_+(\alpha, \delta, \psi; t)h_+(t) + F_\times(\alpha, \delta, \psi; t)h_\times(t), \quad (3)$$

where $F_+(\alpha, \delta, \psi; t)$ and $F_\times(\alpha, \delta, \psi; t)$ are the detector beam pattern functions and

$$\begin{aligned} h_+(t) &= A_+ \cos \Phi(t) \\ h_\times(t) &= A_\times \sin \Phi(t). \end{aligned} \quad (4)$$

If ι is the angle between the total angular momentum of the star and the direction from the star to Earth

$$\begin{aligned} A_+ &= \frac{1}{2}h_0(1 + \cos^2 \iota) \\ A_\times &= h_0 \cos \iota. \end{aligned} \quad (5)$$

h_0 is the intrinsic gravitational-wave amplitude, (α, δ) are the right-ascension and declination for the source, and ψ is the orientation of the wave-frame with respect to the detector frame. Due to Earth's motion, the orientation between the detector and the source is changing all the time, which makes $F_{+, \times}$ time-varying. $\Phi(t)$ is the phase of the gravitational-wave signal at time t . If with τ we indicate the arrival time of the wave with phase $\Phi(t)$ at the solar system barycenter (SSB), then

$$\begin{aligned} \Phi(\tau) &= \Phi_0 + 2\pi[f(\tau - \tau_{\text{ref}}) + \\ &\quad \frac{1}{2}\dot{f}(\tau - \tau_{\text{ref}})^2 + \frac{1}{6}\ddot{f}(\tau - \tau_{\text{ref}})^3 + \dots]. \end{aligned} \quad (6)$$

If the frequency derivatives are non-zero, the reference time τ_{ref} (or t_{ref}) determines the frequency scale. The transformation between detector time t and solar system barycenter time τ is

$$\tau(t) = t + \frac{\mathbf{r}(t) \cdot \mathbf{n}}{c} + \Delta_{\text{E}\odot} - \Delta_{\text{S}\odot}, \quad (7)$$

where $\mathbf{r}(t)$ is the position vector of the detector in the SSB frame, \mathbf{n} is the unit vector pointing to the source, and c is the speed of light; $\Delta_{\text{E}\odot}$ and $\Delta_{\text{S}\odot}$ are respectively the relativistic Einstein and Shapiro time delays. We refer the reader to (Jaranowski et al. 1998) for further details.

4.3. The signal-parameter ranges

The position of PSR J0537-6910 is known with high accuracy, so if we knew precisely its spin frequency ν and its derivatives $\dot{\nu}$, $\ddot{\nu}$, from Eq. (2) we could determine the range of possible values of the r-mode gravitational-wave frequency f and its derivatives \dot{f} , \ddot{f} . However, since there are no timing data available for the O1 and O2 data period (Antonopoulou et al. 2018), ν , $\dot{\nu}$, $\ddot{\nu}$ are not known precisely.

For each search we set the reference time t_{ref} in the middle of each observation period. At that reference time we determine the range of values for $\nu \in [\nu_{\text{min}}, \nu_{\text{max}}]$, $\dot{\nu} \in [\dot{\nu}_{\text{min}}, \dot{\nu}_{\text{max}}]$ and $\ddot{\nu} \in [\ddot{\nu}_{\text{min}}, \ddot{\nu}_{\text{max}}]$. From Eq. 2 the corresponding gravitational-wave frequency and derivatives ranges are then

$$\left\{ \begin{array}{l} \left(1.39 - 0.195 \frac{\nu^2}{\nu_K^2} \right) \Big|_{\nu_{\text{min}}} \quad \nu_{\text{min}} \leq f \leq 1.57 \nu_{\text{max}} \\ \left(1.39 - 0.585 \frac{\nu^2}{\nu_K^2} \right) \Big|_{\nu_{\text{max}}} \quad |\dot{\nu}|_{\text{min}} \leq |\dot{f}| \leq 1.57 |\dot{\nu}|_{\text{max}} \\ \left(0.9929 - 0.4179 \frac{\nu^2}{\nu_K^2} \right) \Big|_{\nu_{\text{max}}} \quad \ddot{\nu}_{\text{min}} \leq \ddot{f} \leq 1.57 \ddot{\nu}_{\text{max}}. \end{array} \right. \quad (8)$$

The range of possible values for ν and $\dot{\nu}$ stems from our ignorance on when glitches occurred, bracketing the gravitational-wave observations. If we assume that there is r-mode emission throughout our observation periods, then the spin state of the star at each t_{ref} only depends on how long before t_{ref} , the previous glitch happened. We consider two extremes: 1) r-mode emission sets-in just at the beginning of our observation period and lasts for a very long time; 2) r-mode emission sets-in a long time before the beginning of our observations and ends at the end of the observation period, Fig. (3).

How long is the longest time that we can reasonably consider? We take the longest known inter-glitch period, ≈ 284 days, and imagine that for scenario 1) r-mode emission starts with our observations and lasts (284 –

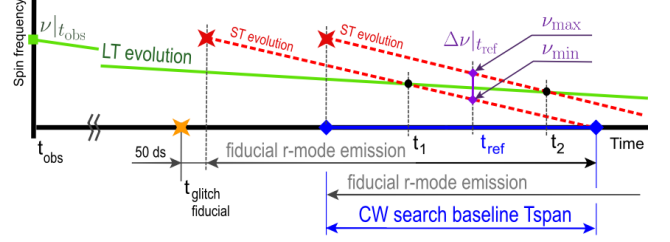


Figure 3. Spin evolution of the PSR J0537-6910 under the two different scenarios discussed in the text.

50) days, at which time the next glitch happens; for scenario 2) r-mode emission starts (284 – 50 – T_{span}) days before the beginning of the observation period (where T_{span} is the duration of the gravitational-wave observation in days). In these two cases the inter-glitch epochs, i.e. the mid-times in-between two successive glitches, are

$$\begin{cases} t_1 = t_0^{\text{gw}} + 92 \text{ days} \\ t_2 = t_0^{\text{gw}} + T_{\text{span}} - 142 \text{ days}, \end{cases} \quad (9)$$

with t_0^{gw} being the time corresponding to the start of the gravitational-wave observation period and the subscripts “1” and “2” indicating the two different scenarios. Consistently with (Antonopoulou et al. 2018) we can then determine the signal parameters at t_1 and t_2 by evolving the values of Tab. 1 defined at the last observed inter-glitch epoch t_{obs} with n_{LT} , $\ddot{\nu}_{\text{LT}}$. We obtain $\nu|_{t_1}^{\text{LT}}$ and $\nu|_{t_2}^{\text{LT}}$. Since $\nu|_{t_1}^{\text{ST}} \equiv \nu|_{t_1}^{\text{LT}}$, $\nu|_{t_2}^{\text{ST}} \equiv \nu|_{t_2}^{\text{LT}}$, we use these values to derive the ones at the reference time for each search $t_{\text{ref}} = t_0^{\text{gw}} + \frac{1}{2} T_{\text{span}}$, by evolving them according to the short term (ST) evolution model of Tab. 1. Specifically, we consider n_{ig} , $\ddot{\nu}_{\text{ig}}^{\text{min}}$ and $\ddot{\nu}_{\text{ig}}^{\text{max}}$ and from these, using the definition of braking index, we derive $\dot{\nu}(t_1, n_{\text{ig}}, \ddot{\nu}_{\text{ig}}^{\text{min}})$, $\dot{\nu}(t_2, n_{\text{ig}}, \ddot{\nu}_{\text{ig}}^{\text{min}})$, $\dot{\nu}(t_1, n_{\text{ig}}, \ddot{\nu}_{\text{ig}}^{\text{max}})$ and $\dot{\nu}(t_2, n_{\text{ig}}, \ddot{\nu}_{\text{ig}}^{\text{max}})$. We evolve these to t_{ref} and find four values of $\nu(t_{\text{ref}})$ and four values of $\dot{\nu}(t_{\text{ref}})$, corresponding to $(t_1, \ddot{\nu}_{\text{ig}}^{\text{min}})$, $(t_2, \ddot{\nu}_{\text{ig}}^{\text{min}})$, $(t_1, \ddot{\nu}_{\text{ig}}^{\text{max}})$ and $(t_2, \ddot{\nu}_{\text{ig}}^{\text{max}})$. We take ν_{min} , ν_{max} , $\dot{\nu}_{\text{min}}$ and $\dot{\nu}_{\text{max}}$ as the smallest and largest among the four. These quantities define the range of possible spin frequencies and derivatives. We assume that $\ddot{\nu}_{\text{min}} = \ddot{\nu}_{\text{ig}}^{\text{min}}$ and $\ddot{\nu}_{\text{max}} = \ddot{\nu}_{\text{ig}}^{\text{max}}$.

The reference times for each observation period O1, O2.1 and O2.2 are given in Table 4 and the corresponding boundaries for the spin frequency and spindown in Table 2:

All these values can be substituted in Eq. (8) and finally yield the gravitational-wave frequency and frequency derivative search ranges shown in Table 3.

Table 2. The range of spin frequency and frequency-derivatives for PSR J0537-6910 at the reference time of each search. The parameter uncertainties from Table 1 are propagated throughout the derivations described in the text and are indicated with brackets.

Search run	O1	O2.1	O2.2
ν_{\min} [Hz]	61.9344(10)	61.9261(14)	61.9236(15)
ν_{\max} [Hz]	61.9365(9)	61.9294(11)	61.9266(12)
$\dot{\nu}_{\min}$ [Hz/s]		$-4.22(27) \times 10^{-10}$	
$\dot{\nu}_{\max}$ [Hz/s]		$-2.02(11) \times 10^{-10}$	
$\ddot{\nu}_{\min}$ [Hz/s ²]		$4.89(7) \times 10^{-21}$	
$\ddot{\nu}_{\max}$ [Hz/s ²]		$2.13(7) \times 10^{-20}$	

Table 3. The search parameter space. The brackets indicate uncertainties.

Search run	O1	O2.1	O2.2
f_{\min} [Hz]	85.9078(14)	85.8964(19)	85.8929(20)
f_{\max} [Hz]	97.2403(13)	97.2291(17)	97.2247(19)
Δf [Hz]	11.3325(19)	11.3327(25)	11.3318(28)
\dot{f}_{\min} [Hz/s]		$-6.63(43) \times 10^{-10}$	
\dot{f}_{\max} [Hz/s]		$-2.79(15) \times 10^{-10}$	
$\Delta \dot{f}$ [Hz/s]		$3.84(45) \times 10^{-10}$	
\ddot{f}_{\min} [Hz/s ²]		$4.82(7) \times 10^{-21}$	
\ddot{f}_{\max} [Hz/s ²]		$3.34(11) \times 10^{-20}$	
$\Delta \ddot{f}$ [Hz/s ²]		$2.86(11) \times 10^{-20}$	

4.4. Detection statistics

We perform a fully coherent, multi-detector search using a maximum likelihood matched filtering method known as \mathcal{F} -statistic (Cutler & Schutz 2005). The \mathcal{F} -statistic is the optimal frequentist statistic for this type of signal, in the presence of stationary, Gaussian detector noise. The resulting detection values, $2\mathcal{F}$, for each template represent the likelihood that a signal with the template’s waveform be present in the data, with respect to Gaussian noise. In Gaussian noise $2\mathcal{F}$ follows a χ^2 -distribution with 4 degrees of freedom (χ_4^2) and a non-centrality parameter that equals the squared signal-to-noise ratio (Jaranowski et al. 1998).

In the presence of spectral disturbances in the data, the detection statistic can be improved by extending the noise model to include “noise lines”, on top of Gaussian noise (Keitel et al. 2014). The corresponding line-robust statistic \hat{B}_{SGL} requires the choice of the tuning parameter $\mathcal{F}_*^{(0)}$ that defines the single-detector \mathcal{F} -statistic magnitude at which \hat{B}_{SGL} begins to down-rank search results with respect to the pure Gaussian noise model. $\mathcal{F}_*^{(0)}$ is usually defined in terms of a Gaussian-noise false-alarm probability $\chi^2(2\mathcal{F}_*^{(0)}|0)$, which we choose to be $\approx 1/N^{\text{eff}}$, the effective number of independent templates. The results of the search are ranked according to \hat{B}_{SGL} . For this search we estimate that $N^{\text{eff}} = 0.9 N_{\text{tot}}$, where N_{tot} is the total number of searched templates.

4.5. The search set up

The search targets different wave shapes, each defined by a value of the gravitational-wave frequency and frequency-derivatives, f, \dot{f}, \ddot{f} . The ensemble of waveforms obtained by varying the values for the f, \dot{f}, \ddot{f} within the boundaries given by Table 3, constitutes the signal template bank of our search.

Table 4. Parameters of each search, including the template grid spacings, the start and reference times t_0^{gw} and t_{ref} , the search time-baseline T_{span} , the total time for which there is data from both detectors T_{data} (expressed as the total number of input SFTs), an estimate of the number of independent templates N^{eff} and the tuning parameter $\mathcal{F}_*^{(0)}$.

Search run	O1	O2.1	O2.2
t_0^{gw} [GPS]	1126623625	1167983370	1180975619
t_{ref} [GPS]	1131937856	1170799164	1184354596
T_{span} [days]	123.0	65.2	78.2
T_{data} [N_{SFT}]	6287	4107	4790
δf [Hz]	3.05×10^{-08}	5.77×10^{-08}	4.8×10^{-08}
$\delta \dot{f}$ [Hz/s]	2.22×10^{-14}	7.92×10^{-14}	5.5×10^{-14}
$\delta \ddot{f}$ [Hz/s ²]	9.89×10^{-21}	6.65×10^{-20}	3.85×10^{-20}
$\log_{10} N^{\text{eff}}$	13.3	12.0	12.2
$\mathcal{F}_*^{(0)}$	34.2	31.1	31.6

The grid spacings ($\delta f, \delta \dot{f}, \delta \ddot{f}$) are such that the average loss in detection efficiency due to signal-template mismatch is about 6%. The mismatch distribution is shown Fig. 4. The details of the procedure can for instance be found in (Behnke et al. 2015). Since the $\delta \ddot{f}$ spacing is smaller than \dot{f}_{\min} from Eq.s 8, we set $\dot{f}_{\min} = 0$.

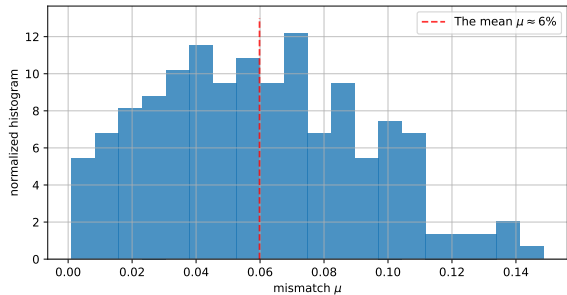


Figure 4. The mismatch distribution μ for the search template grid computed from 200 searches on fake signals. $\mu = \frac{\rho_{\text{PM}}^2 - \rho_{\text{grid}}^2}{\rho_{\text{PM}}^2}$ with ρ^2 being the signal-to-noise measured with a perfect match between signal and template (“PM”) and with a search over the original search grid (“grid”).

A summary of all search parameters is given in Table 4. Overall, we search $\approx 10^{13}$ templates in every search.

5. RESULTS

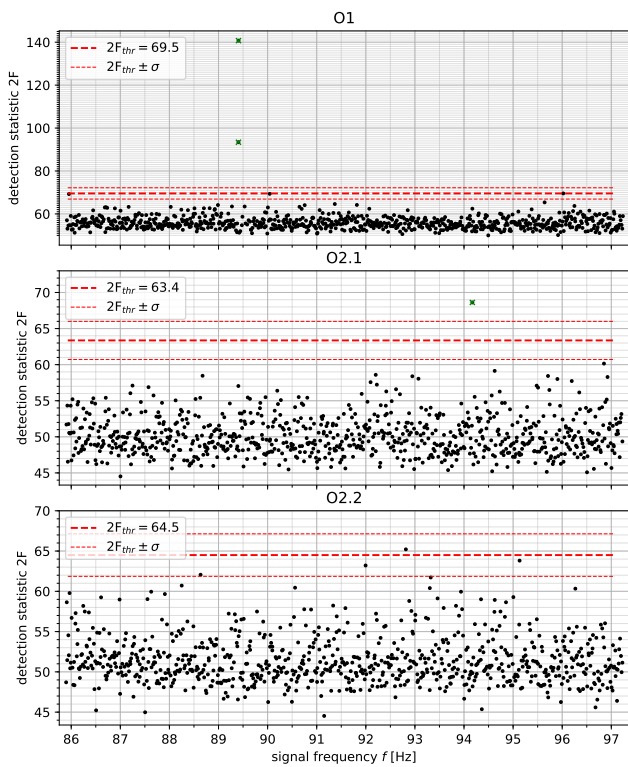


Figure 5. The most significant candidate in every 0.014 Hz band. We note the value of $2\mathcal{F}_{\text{thr}}$ for each search, the expected highest detection statistic value in Gaussian noise over the number of independent templates searched.

Fig. 5 shows the $2\mathcal{F}$ values of the most significant \hat{B}_{SGL} results in every 0.014 Hz band, after having excluded results close to spectral artefacts that were

cleaned-out in the input data (Covas et al. 2018; Abbott et al. 2017). The cleaning procedure substitutes the real data with fake Gaussian noise, hence these data do not contribute any astrophysical information to the results. The extent of the excluded region is determined by the extent of the original spectral contamination and by an evaluation of the spread that this would generate in signal-frequency space, for our specific target and for the largest searched $|f|$. This removes 3.6% (O1), 2.2% (O2.1) and 3% (O2.2) of the results. The complete list of the bands excluded from further inspection and from the upper limit statements, is given in appendix A.

We compare the $2\mathcal{F}$ values with $2\mathcal{F}_{\text{thr}}$, the expected most significant $2\mathcal{F}$ over the entire search in Gaussian noise:

$$2\mathcal{F}_{\text{thr}} = \int_0^\infty \chi_4^2 N^{\text{eff}} F_{\chi_4^2}^{(N^{\text{eff}}-1)} p_{\chi_4^2} d\chi_4^2, \quad (10)$$

where $p_{\chi_4^2}$ is the probability density function of a χ_4^2 variable and $F_{\chi_4^2}$ its cumulative distribution. We do not use $2\mathcal{F}_{\text{thr}}$ as a rigorous measure of significance but rather as an indicator.

If a candidate were found well above $2\mathcal{F}_{\text{thr}}$ with consistent parameters across the three searches, this would *not* automatically mean that it is a signal from J0537-6910, but it would certainly warrant further investigation. On the other hand, if no consistent candidate exists above the expected loudest, it is unlikely that we can confidently identify a signal with this search.

We find ten candidates with $2\mathcal{F} \geq 2\mathcal{F}_{\text{thr}} - \sigma$, and they are listed in Table 5. We comment only on the three that exceed at least the $+1\sigma$ level.

O1 search: There are two outstanding candidates at ≈ 89.41 Hz whose detection statistic exceeds the expectation for the loudest by about 9σ and 27σ , respectively. Their proximity in frequency indicates that the two candidates are due to the same root cause, which we identify in spectral disturbances in the Hanford detector. This is also clearly reflected in the results of an all-sky search on the same data (Abbott et al. 2017): the distribution over sky position of the top results from that search is typical of a disturbance rather than of a signal or of Gaussian noise, and the results at the position of J0537-6910 are not significant in any way. Figure 6a illustrates our findings.

O2.1 search: The most significant candidate at 94.17 Hz is $\approx 2\sigma$ above the expectation. The all-sky search around this frequency doesn’t reveal any disturbance, as shown in Figure 6b. The average noise of the detectors at the relevant frequencies does not exhibit any notable feature.

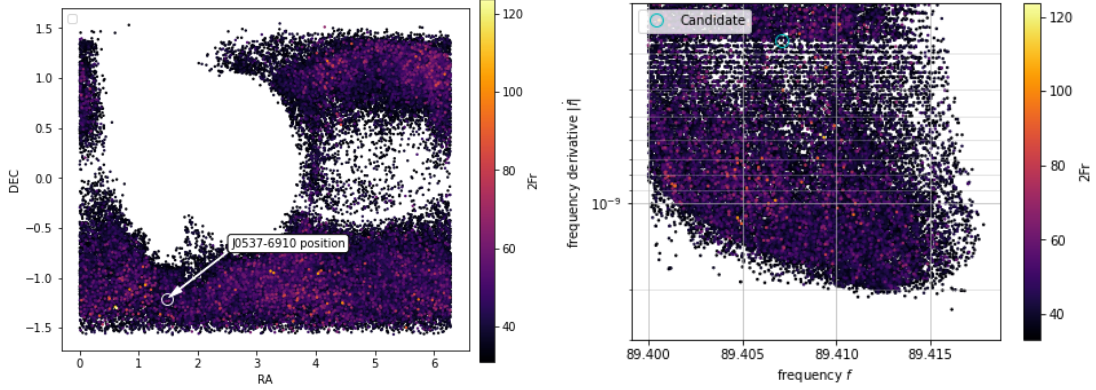
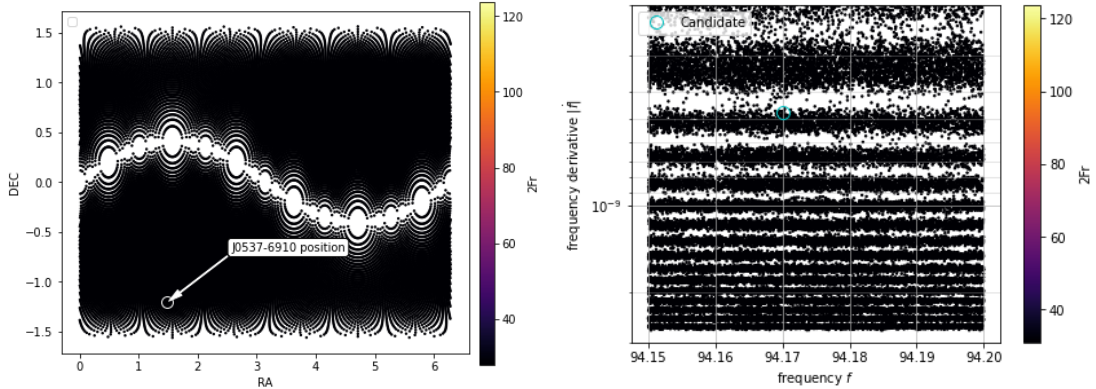

 (a) Candidate in O1 at $f = 89.4071$ Hz

 (b) Candidate in O2.1 at $f = 94.17$ Hz

Figure 6. Results of the all-sky O1 and O2 searches (Abbott et al. 2017; Steltner et al. 2020) in the parameter regions of the two candidates of Table 5. The plots show the detection statistic values (color-coded) as a function of the template-waveform frequency and frequency derivative in the top panels, and as a function of the template-waveform source position (α, δ) in the bottom panels. When a spectral region is contaminated, the distribution of candidates is not uniform in parameter space, and this can be clearly seen in panel (a), as opposed to panel (b) that portrays results from an undisturbed frequency region.

O2.2 search: There are no significant candidates from this search: all the listed candidates are within 1σ of the expectations.

5.1. Upper limits on the gravitational-wave amplitude

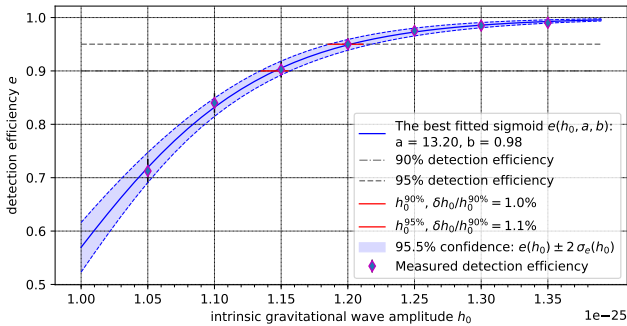


Figure 7. Detection efficiency curve for the band 87.75 – 88.25 Hz in O2.1 search run. This is a typical result.

We set upper limits on the intrinsic gravitational amplitude h_0 in 0.5 Hz bands, based on the highest detection statistic value measured in each band, after the results from the fake Gaussian noise bands are removed. We perform 200 fake-signal search-and-recovery Monte Carlo within each band. The signals are all at the location of J0537-6910, with frequency, spindown and initial phase values taken from uniform random distributions in their respective ranges. We add these signals in the real data. We consider values of h_0 ranging from 9.5×10^{-26} to 1.8×10^{-25} .

The searches are performed with the same grids and set-up as the search, Tab. 3, in the neighbourhood of the fake signal parameters. A signal is counted as recovered if the highest detection statistic value from the fake-signal search is higher than the one recorded in the actual search. The detection efficiency $e(h_0)$ is the fraction of recovered signals.

We adopt a sigmoid of the form $e(h_0) = (1 + \exp(\frac{a-h_0}{b}))^{-1}$ to fit h_0 with the corresponding measured

Table 5. The most significant candidates from each of the searches.

f [Hz]	\dot{f} [Hz/s]	\ddot{f} [Hz/s ²]	$2\mathcal{F}$	$\frac{2\mathcal{F}-2\mathcal{F}_{\text{thr}}}{\sigma}$	\hat{B}_{SGL}
O1					
89.4071	-2.72×10^{-10}	1.96×10^{-20}	140.7	27.0	0.77
96.0229	-6.34×10^{-10}	9.70×10^{-21}	69.5	0.0	0.52
85.9534	-3.41×10^{-10}	9.70×10^{-21}	69.3	-0.1	0.46
90.0425	-4.57×10^{-10}	2.95×10^{-20}	69.4	-0.1	0.44
89.4060	-3.40×10^{-10}	9.70×10^{-21}	93.4	9.0	-0.02
O2.1					
94.1700	-4.72×10^{-10}	1.96×10^{-20}	68.6	2.0	1.67
O2.2					
92.8159	-5.00×10^{-10}	1.96×10^{-20}	65.2	0.3	0.69
95.1321	-6.83×10^{-10}	1.96×10^{-20}	63.8	-0.3	0.38
91.9957	-6.19×10^{-10}	1.96×10^{-20}	63.2	-0.5	0.25
88.6347	-4.71×10^{-10}	1.96×10^{-20}	62.1	-0.9	0.00

detection efficiency. We use Python’s “curve fit” package (Python 2019) based on the Levenberg-Marquardt algorithm through the least squares method. The uncertainties in e stemming from the measurement error on the number of recovered signals are translated in uncertainties on the fit parameters δa and δb , computed as the square root of the diagonal elements of the covariance matrix. We use δa and δb to estimate the standard deviation $\sigma_e(h_0)$ of the best fit sigmoid $e(h_0)$. Fig. 7 shows an example of the sigmoid fit with two curves $e(h_0) \pm 2\sigma_e(h_0)$ that bracket the expected $e(h_0)$ curve with $> 95\%$ confidence.

The 90% confidence upper limit on the intrinsic gravitational-wave amplitude is the smallest h_0 such that 90% of the target signal population in the search range would have produced a value of the detection statistic higher than the one that was measured in the search. We read this value, $h_0^{90\%}$, off the sigmoid fit curve at $e = 0.9$.

The uncertainty δe determines the range of variability for $h_0^{90\%}$ which overall amounts to $\leq 2\%$ of the upper limit value. We add the calibration uncertainty which we conservatively take to be 5% (Cahillane et al. 2017). The upper limits together with their uncertainties are plotted in Fig. 8 for all 3 search runs. They are provided in tabular form in the appendix B and in machine-readable format at (AEI 2020). We also compute the

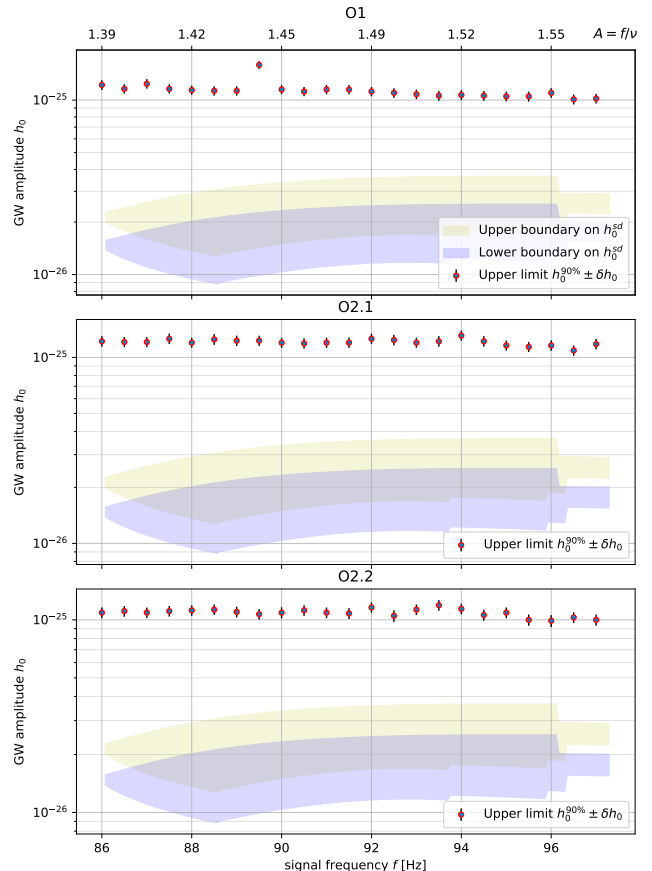


Figure 8. The markers show the upper limits on gravitational-wave amplitude $h_0^{90\%}$ for a continuous signal from J0537-6910 from each of the searches. The shaded regions show the range of values that the spin-down upper limit could take, depending on the equation of state of the star, as described in Section 5.1.2. The second x-axis, on the top, shows $A(f)$ for the $h_0^{\text{sd}}_{\text{max}}$ curve, i.e. $A = f/\nu_{\text{min}}$. On this scale it is however not possible to appreciate the difference with $A = f/\nu_{\text{max}}$, so the plotted axes hold for all quantities shown.

95% confidence upper limits, which are $\lesssim 5\%$ higher than the 90% confidence ones.

5.1.1. Sensitivity depth

The sensitivity depth is a useful measure to compare the baseline performance of different searches (Dreissgacker et al. 2018). It was first introduced in (Behnke et al. 2015) as

$$\mathcal{D}^{90\%}(f) = \frac{\sqrt{S_h(f)}}{h_0^{90\%}(f)} [1/\sqrt{\text{Hz}}], \quad (11)$$

where $\sqrt{S_h(f)}$ is the noise level associated with the signal frequency f . The multi-detector $S_h(f)$ for our searches is the harmonic mean of the single-detector power spectral densities S_h^H and S_h^L of the data, then

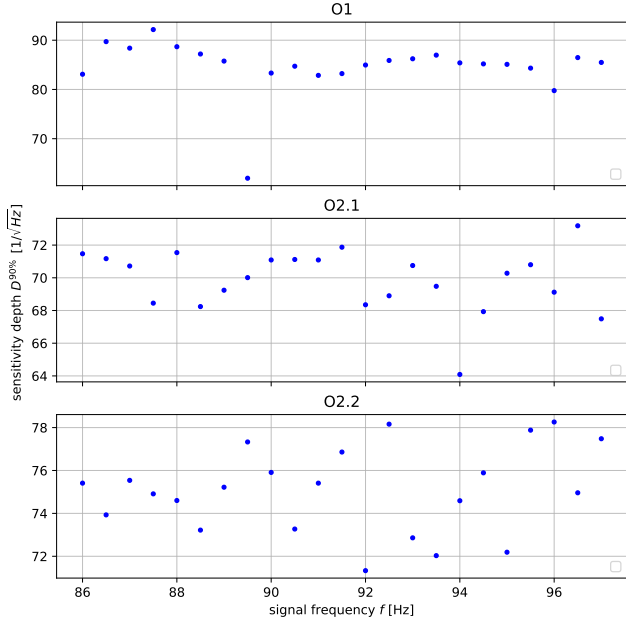


Figure 9. The sensitivity depth

averaged over the 0.5 Hz frequency band that the upper limit value refers to. The resulting $\mathcal{D}^{90\%}(f)$ is shown in Fig. 9 and tabulated in Appendix B. We provide the values of $\sqrt{S_h(f)}$ in machine readable format at (AEI 2020).

5.1.2. Spin-down limit

If all the kinetic energy lost by J0537-6910 (its spin-down) rotating at ν is due to gravitational emission at frequency f , its gravitational-wave amplitude is

$$h_0^{\text{sd}} = \frac{1}{D} \sqrt{\frac{10G}{c^3} I_{zz} \frac{|\dot{\nu}| \nu}{f^2}} \quad (12)$$

where I_{zz} is the moment of inertia of the star with spin axis in the \hat{z} direction. If in Eq.s 1 we neglect the terms in $(\nu/\nu_K)^2$ (slowly rotating star) and set $A = f/\nu$ then

$$h_0^{\text{sd}} = \frac{1}{AD} \sqrt{\frac{10G}{c^3} I_{zz} \frac{|\dot{\nu}|}{\nu}}. \quad (13)$$

This is a general formula that applies to any emission mechanism. If the emission is due to an equatorial ellipticity in the star, then $A = 2$ and we find the commonly-seen spindown-limit formula, for example Eq. 5 of (Aasi et al. 2014).

In the case of r-mode emission A encodes information on the equation of state of the star. As shown in Fig. 10, mass M and radius R are different functions of A for different equations of state. If $\mathcal{C} = M/R$ is the compactness of the star, then $A = |-1.373 + .079\mathcal{C} - 2.25\mathcal{C}^2| \in [1.39; 1.57]$ for $M \in [1.02 - 2.76 M_\odot]$ and compactness

$\mathcal{C} = M/R \in [0.11, 0.31]$. This was found by fitting 14 realistic equations of state by (Idrisy et al. 2015) and we will use it in Eq. 14 to compute $M(A)$ and $R(A)$ from $M(\mathcal{C})$ and $R(\mathcal{C})$ given in (Ozel et al. 2016a,b).

The moment of inertia I_{zz} also depends on the equation of state. We re-write it in terms of the normalized moment of inertia $\tilde{I} := I_{zz}/M^3$ that can be expressed in terms of \mathcal{C} for slowly rotating stars with the coefficients given in Tab. 2 of (Breu & Rezzolla 2016).

Eq. (13) then becomes

$$h_0^{\text{sd}}(A, \frac{|\dot{\nu}|}{\nu}) = \frac{1}{AD} \sqrt{\frac{10G}{c^3} \tilde{I}(A) M^3(A) \frac{|\dot{\nu}|}{\nu}}. \quad (14)$$

We consider two extremes:

$$\begin{cases} h_{0 \min}^{\text{sd}}(A) = h_0^{\text{sd}}(A, \frac{|\dot{\nu}|}{\nu} |_{\min}), & \frac{|\dot{\nu}|}{\nu} |_{\min} = |\dot{\nu}|_{\min} / \nu_{\max} \\ h_{0 \max}^{\text{sd}}(A) = h_0^{\text{sd}}(A, \frac{|\dot{\nu}|}{\nu} |_{\max}), & \frac{|\dot{\nu}|}{\nu} |_{\max} = |\dot{\nu}|_{\max} / \nu_{\min}. \end{cases} \quad (15)$$

As $M(A)$ varies in the range shown in middle panel of Fig. 10, we find the corresponding range $\Delta h_{0 \min}^{\text{sd}}$ and $\Delta h_{0 \max}^{\text{sd}}$. We set $A = f/\nu_{\min}$ in $\Delta h_{0 \max}^{\text{sd}}$ and $A = f/\nu_{\max}$ in $\Delta h_{0 \min}^{\text{sd}}$ and derive the two differently shaded regions of Fig. 8 which define range of variability of the spin-down upper limit h_0^{sd} . We are neglecting the $B\nu^2/\nu_K^2$ term of Eq. 1 for simplicity. This approximation is completely unimportant in the context of sketching the boundaries of h_0^{sd} .

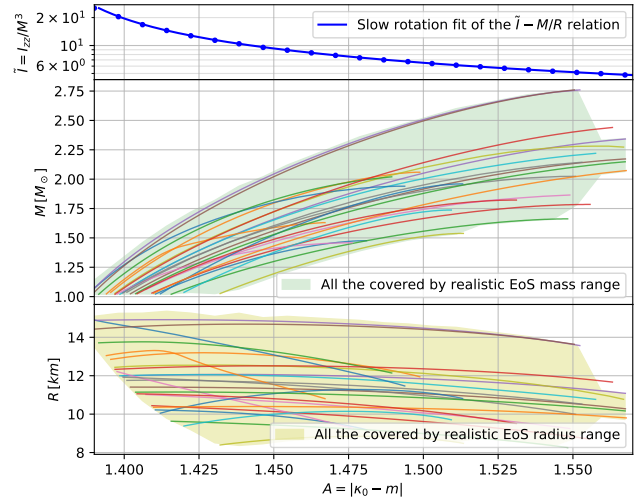


Figure 10. $\tilde{I} - M/R$ Universal relation and ranges of M and R from realistic EoS.

5.2. Upper limits on the r-mode amplitude

The r-mode saturation amplitude α that supports gravitational-wave emission with a strain h_0 at a frequency f from a source at a distance D is (Owen 2010):

$$\alpha = \sqrt{\frac{5}{8\pi}} \frac{c^5}{G} \frac{h_0}{(2\pi f)^3} \frac{D}{MR^3 \tilde{J}}, \quad (16)$$

where \tilde{J} is the dimensionless canonical angular momentum of the r-mode (Owen et al. 1998). \tilde{J} is less dependant on the equation of state than M and R so, following (Owen et al. 1998), we fix its value to 0.0164 (as computed from a polytropic EoS with index $n = 1$) and encapsulate the dependency on the equation of state in the term MR^3 , as function of A .

The gravitational-wave frequency also depends on A : $f = A\nu$. As done in Section 5.1.2 we consider

$$\begin{cases} \alpha^{\min}(h_0, A, f = A\nu_{\max}) = \sqrt{\frac{5}{8\pi}} \frac{c^5}{G} \frac{h_0}{(2\pi A\nu_{\max})^3} \frac{D}{M(A)R(A)^3 \tilde{J}} \\ \alpha^{\max}(h_0, A, f = A\nu_{\min}) = \sqrt{\frac{5}{8\pi}} \frac{c^5}{G} \frac{h_0}{(2\pi A\nu_{\min})^3} \frac{D}{M(A)R(A)^3 \tilde{J}} \end{cases} \quad (17)$$

and for each of these curves the range $A \in [1.39, 1.57]$ determines the range of variability of the saturation amplitude α as a function of h_0 . In practice since $\alpha^{\min}(h_0, A, f = A\nu_{\max}) \approx \alpha^{\max}(h_0, A, f = A\nu_{\min})$ we convert the gravitational-wave amplitude upper-limits $h_0^{90\%}$ to ranges for the r-mode amplitude upper limits in every half Hz bands as

$$\alpha^{90\%}(f) = \alpha(h_0^{90\%}, A, f = A\nu_{\min}), \quad A \in [1.39, 1.57]. \quad (18)$$

The results are shown on Fig. (11) for all search runs. The shaded area represent the spread of α in the possible range of $M(A)R(A)^3$ bounded by realistic equations of state, as well as the upper limit for $M = 1.4 M_\odot$, $R = 11.7$ km (middle black curve).

5.3. Not always “ON” signal

Our upper limits are based on the optimistic assumption that the r-mode signal is always “ON” during the time of the searches. This might not be the case because in the model that we consider, r-mode emission begins some time after a glitch and ends with the next glitch. Not knowing when glitches happened for J0537-6910 around the O1 and O2 observing times, we cannot be sure that some of our search times do not fall in a period too close to a glitch to be emitting r-modes, according to our model. In order to estimate the impact of this assumption we randomly pick start times for the O1 and O2 runs during the 13 years for which we have glitch-occurrence times and based on this glitch-time, we compute the fraction of these simulated O1, O2.1 and O2.2 runs which overlaps with the r-mode emission period¹. The resulting distributions for 1000 draws of the

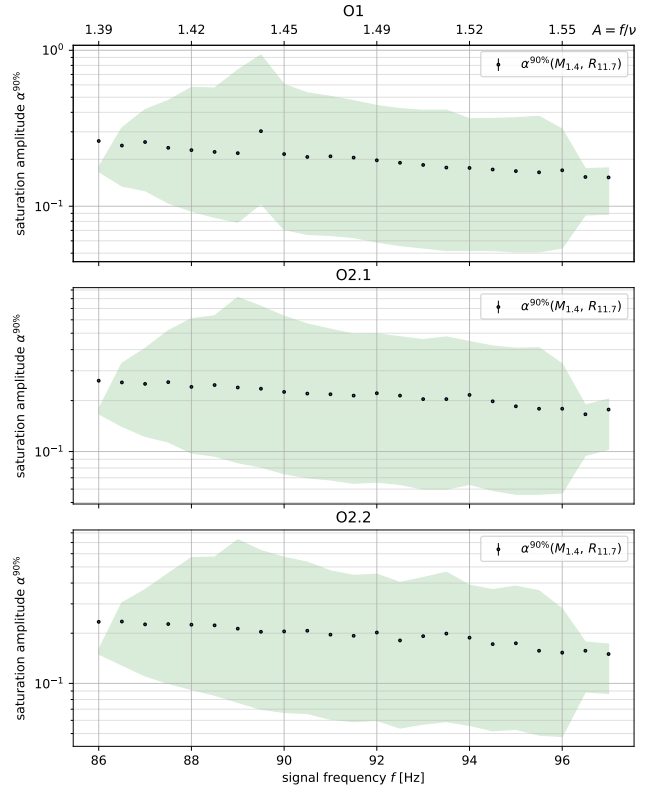


Figure 11. Upper limits on the r-mode saturation amplitude α derived from the gravitational-wave amplitude upper limits $h_0^{90\%}$.

start times are shown in the top panel of Fig. 12. Since the data has gaps which are not uniformly distributed, the fraction of the overlapping *time* is not equal to the fraction of *data* in the overlap stretches, so we also compute this and show the distributions in the bottom panel of Fig. 12. We find that the 50th percentiles for the overlap fraction of the data are $\approx 45\%$ for O1 and $\approx 50\%$ for O2.1 and O2.2. We repeat the simulation-and-search Monte Carlo described in Section 5.1 for O1, O2.1 and O2.2 with signals from this population and with frequency between 87.75 Hz and 88.25 Hz. In this sample frequency band we find a $h_0^{90\%}$ higher by a factor $\approx 4.4, 3.7$ and 4.2 respectively for the three searches, compared to the always-ON-signal results.

6. CONCLUSIONS

Pulsar J0537-6910 is an intriguing candidate for r-mode gravitational-wave emission $\gtrsim 50$ days after a glitch. Unfortunately we do not know whether the object glitched during the O1 and O2 LIGO data runs, so we carry out three coherent searches for r-mode continuous gravitational waves on periods lasting several tens of days. We choose the periods based on the available data and its gaps. We pick the frequency and

¹ We recall that we have defined the r-mode emission period to be the period 50-day after a glitch to the next glitch.

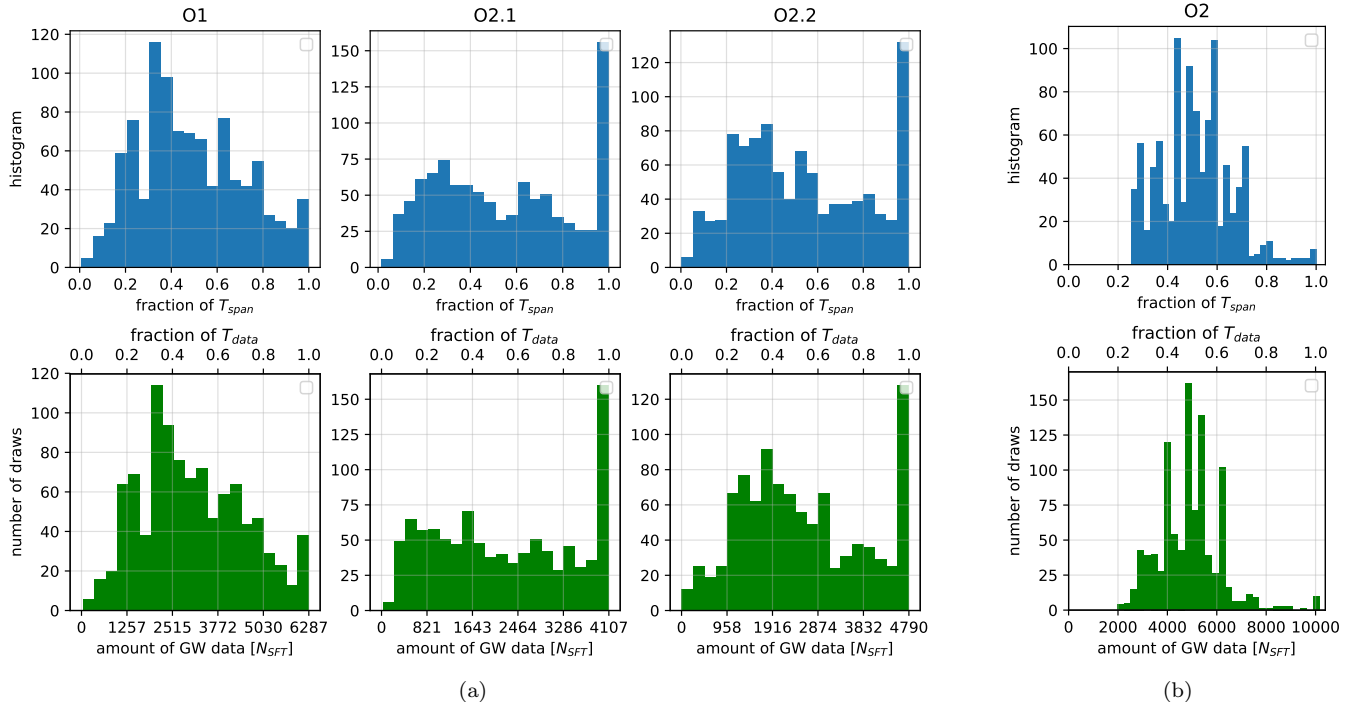


Figure 12. Distributions of the fraction of the searches’ observation spans T_{span} (top panels) and distribution of the amount of gravitational-wave data T_{data} (lower panels) that overlap with the longest glitch-free period (for O2). The amount of data is expressed by the number of input SFTs (N_{SFT}). The total number of SFTs is given in Tab. 4 as T_{data} for O1, O2.1, O2.2, and $T_{\text{data}} = 10194 N_{\text{SFT}}$ for O2. These r-mode emission periods are simulated by drawing 1000 random search start-times during the 13 years for which we have the occurrence-time of J0537-6910 glitches.

frequency-derivative range to be large enough to include all uncertainties in the rotation frequency timing model, evolved to the time of the observations, and the uncertainties stemming from the unknown equation of state of the star. This is the first search specifically targeting r-mode emission from a known pulsar. While we do not find evidence for a continuous gravitational-wave signal, we report a marginal outlier from the O2.1 search at ~ 94.17 Hz. We set upper limits on the gravitational-wave amplitude of r-mode signals in 0.5 Hz bands. Overall, the h_0 upper limits span a range between $(1 - 1.6) \times 10^{-25}$, with an average sensitivity depth between 75 and $85 \frac{1}{\sqrt{\text{Hz}}}$, consistent with the size of the data sets employed. The r-mode saturation amplitude values that this search could detect are consistent with those necessary to interpret the EM observations in terms of unstable r-mode emission (Andersson et al. 2018). They are about an order of magnitude larger than the physically most plausible ones but scenarios can be imagined where even such high values are possible. We refer the reader to the discussion on this point in Section 3 of (Andersson et al. 2018). Our upper limits are a factor of ≈ 5 higher than the average spin-down limit amplitude.

Lacking precise ephemeris data for this pulsar, J0537-6910 was not included in the LIGO 220+ known-pulsars search (Abbott et al. 2019c), but was later targeted in a small, 0.25 Hz search around twice the rotation frequency, 123.86 Hz, in (Abbott et al. 2019a). That search, carried out on the O2 data, is limited to a spin-down range of 8×10^{-13} Hz/s and overall comprises $\sim 1.6 \times 10^9$ templates, about 10000 times fewer than employed here for each of our searches. The upper limits of (Abbott et al. 2019a) are consistent with the longer coherent time-baseline, the different level of the detector noise and the significantly smaller template bank of that search with respect to the one presented here.

As in (Abbott et al. 2019a), our upper limits are based on the optimistic assumption that the r-mode signal is always “ON” during the time of the searches. Based on historical glitch-occurrence times we construct a population of signals with varying durations and overlaps with our data-sets, and evaluate the upper-limits on this population of signals. The sensitivity is degraded with respect to the always-ON population by a factor ≈ 4 .

The likelihood of a glitch occurring during the 232 days observation time of the LIGO search (Abbott et al. 2019a) is reflected in a mean overlap of the observation

time with the longest inter-glitch periods of 50% (see Fig. 12). (Abbott et al. 2019a) do not comment on their loss of sensitivity due to a possible glitch of J0537-6910. We estimate that for a realistically glitching signal the upper limit $h_0^{95\%}$ of (Abbott et al. 2019a) would be ≈ 3.6 times higher, comparable to the degradation that we report for our searches. Timing of J0537-6910 in order to identify the times when glitches occur, eliminates all these uncertainties and is of paramount importance to search for continuous gravitational waves from J0537-6910.

A very interesting candidate from this search would be a high-significance signal consistent in at least two of the three searches. This would indicate a repeating phenomenon exciting the star’s r-mode instability, coherent with the observations of (Andersson et al. 2018). A definitive confirmation would need a verification on a different gravitational-wave data set, corroborated by glitch information from EM observations. This reinforces the importance of EM timing of J0537-6910.

A detection would be of great importance for multiple reasons. It would be i) the first detection of a continuous gravitational-wave signal, opening interesting prospects for high-precision tests of gravity ii) the first direct observation of gravitational-waves emission through unstable r-modes, as predicted in (Andersson 1998) iii) the discovery that at least some young neutron stars lose angular momentum due to r-mode gravitational waves iv) a probe of neutron star interior.

As new and more sensitive gravitational-wave data becomes available, deeper searches will be possible,

also including the use of specific techniques on longer data sets (Keitel 2016; Keitel & Ashton 2018; Ashton et al. 2018). The scientific return of gravitational-wave searches like this is greatly enhanced when timing data is available, that identifies the rotation parameters during the gravitational-wave observations and glitch-occurrence times. NICER (NICER 2017) could provide this invaluable information to the broad scientific community.

7. ACKNOWLEDGMENTS

We thank Wynn Ho for useful discussions in the early phases of this project, Danai Antonopoulou for having supplied us with the numerical values of Table 1 and 2 of (Antonopoulou et al. 2018), Benjamin Steltner for having prepared the input data for this search, and Heinz-Bernd Eggenstein and the Einstein@Home team for access to the all-sky search results. We acknowledge David Keitel for his comments on our presentation at the 30th Texas Symposium in Portsmouth. A special thank-you to Nils Andersson for the many interesting discussions and for his comments on the manuscript.

This research has made use of data and web tools for data transfer of the gravitational-wave Open Science Center (LIGO 2018d), a service of LIGO Laboratory, the LIGO Scientific Collaboration and the Virgo Collaboration. LIGO is funded by the U.S. National Science Foundation. Virgo is funded by the French Centre National de Recherche Scientifique (CNRS), the Italian Istituto Nazionale della Fisica Nucleare (INFN) and the Dutch Nikhef, with contributions by Polish and Hungarian institutes.

REFERENCES

- Aasi, J., Abadie, J., Abbott, B. P., et al. 2014, *Astrophys. J.*, 785, 119, doi: [10.1088/0004-637X/785/2/119](https://doi.org/10.1088/0004-637X/785/2/119)
- Aasi, J., Abbott, B. P., Abbott, R., et al. 2015, *Class. Quant. Grav.*, 32, 074001, doi: [10.1088/0264-9381/32/7/074001](https://doi.org/10.1088/0264-9381/32/7/074001)
- Abbott, B. P., Abbott, R., Abbott, T. D., et al. 2019a, *Phys. Rev.*, D99, 122002, doi: [10.1103/PhysRevD.99.122002](https://doi.org/10.1103/PhysRevD.99.122002)
- Abbott, B. P., Abbott, R., Adhikari, R., et al. 2009, *Rept. Prog. Phys.*, 72, 076901, doi: [10.1088/0034-4885/72/7/076901](https://doi.org/10.1088/0034-4885/72/7/076901)
- Abbott, B. P., Abbott, R., Abbott, T. D., et al. 2016, *Phys. Rev. Lett.*, 116, 131103, doi: [10.1103/PhysRevLett.116.131103](https://doi.org/10.1103/PhysRevLett.116.131103)
- . 2017, *Phys. Rev.*, D96, 122004, doi: [10.1103/PhysRevD.96.122004](https://doi.org/10.1103/PhysRevD.96.122004)
- . 2019b, *Phys. Rev.*, X9, 031040, doi: [10.1103/PhysRevX.9.031040](https://doi.org/10.1103/PhysRevX.9.031040)
- . 2019c, *Astrophys. J.*, 879, 10, doi: [10.3847/1538-4357/ab20cb](https://doi.org/10.3847/1538-4357/ab20cb)
- AEI. 2020, Supplementary material for the publication, <https://www.aei.mpg.de/continuouswaves/j0537>
- Alford, M. G., & Schwenzer, K. 2014, *Astrophys. J.*, 781, 26, doi: [10.1088/0004-637X/781/1/26](https://doi.org/10.1088/0004-637X/781/1/26)
- . 2015, *Mon. Not. Roy. Astron. Soc.*, 446, 3631, doi: [10.1093/mnras/stu2361](https://doi.org/10.1093/mnras/stu2361)
- Allen, B., & Mendell, G. 2004, SFT Data Format Version 2 Specification, <https://dcc.ligo.org/LIGO-T040164/public>
- Andersson, N. 1998, *Astrophys. J.*, 502, 708, doi: [10.1086/305919](https://doi.org/10.1086/305919)

- Andersson, N., Antonopoulou, D., Espinoza, C. M., Haskell, B., & Ho, W. C. G. 2018, *Astrophys. J.*, 864, 137, doi: [10.3847/1538-4357/aad6eb](https://doi.org/10.3847/1538-4357/aad6eb)
- Andersson, N., Kokkotas, K. D., & Schutz, B. F. 1999, *Astrophys. J.*, 510, 846, doi: [10.1086/306625](https://doi.org/10.1086/306625)
- Antonopoulou, D., Espinoza, C. M., Kuiper, L., & Andersson, N. 2018, *Mon. Not. Roy. Astron. Soc.*, 473, 1644, doi: [10.1093/mnras/stx2429](https://doi.org/10.1093/mnras/stx2429)
- Ashton, G., Prix, R., & Jones, D. I. 2018, *Phys. Rev.*, D98, 063011, doi: [10.1103/PhysRevD.98.063011](https://doi.org/10.1103/PhysRevD.98.063011)
- Behnke, B., Papa, M. A., & Prix, R. 2015, *Phys. Rev.*, D91, 064007, doi: [10.1103/PhysRevD.91.064007](https://doi.org/10.1103/PhysRevD.91.064007)
- Breu, C., & Rezzolla, L. 2016, *Mon. Not. Roy. Astron. Soc.*, 459, 646, doi: [10.1093/mnras/stw575](https://doi.org/10.1093/mnras/stw575)
- Cahillane, C., Betzwieser, J., Brown, D. A., et al. 2017, *Phys. Rev.*, D96, 102001, doi: [10.1103/PhysRevD.96.102001](https://doi.org/10.1103/PhysRevD.96.102001)
- Caride, S., Inta, R., Owen, B. J., & Rajbhandari, B. 2019, *Phys. Rev.*, D100, 064013, doi: [10.1103/PhysRevD.100.064013](https://doi.org/10.1103/PhysRevD.100.064013)
- Covas, P. B., Effler, A., Goetz, E., et al. 2018, *Phys. Rev.*, D97, 082002, doi: [10.1103/PhysRevD.97.082002](https://doi.org/10.1103/PhysRevD.97.082002)
- Cutler, C., & Schutz, B. F. 2005, *Phys. Rev.*, D72, 063006, doi: [10.1103/PhysRevD.72.063006](https://doi.org/10.1103/PhysRevD.72.063006)
- Dreissigacker, C., Prix, R., & Wette, K. 2018, *Phys. Rev.*, D98, 084058, doi: [10.1103/PhysRevD.98.084058](https://doi.org/10.1103/PhysRevD.98.084058)
- Friedman, J. L., & Morsink, S. M. 1998, *Astrophys. J.*, 502, 714, doi: [10.1086/305920](https://doi.org/10.1086/305920)
- Glendenning, N. K. 1992, *Phys. Rev. D*, 46, 4161, doi: [10.1103/PhysRevD.46.4161](https://doi.org/10.1103/PhysRevD.46.4161)
- Idrisy, A., Owen, B. J., & Jones, D. I. 2015, *Phys. Rev.*, D91, 024001, doi: [10.1103/PhysRevD.91.024001](https://doi.org/10.1103/PhysRevD.91.024001)
- Jaranowski, P., Krolak, A., & Schutz, B. F. 1998, *Phys. Rev.*, D58, 063001, doi: [10.1103/PhysRevD.58.063001](https://doi.org/10.1103/PhysRevD.58.063001)
- Keitel, D. 2016, *Phys. Rev.*, D93, 084024, doi: [10.1103/PhysRevD.93.084024](https://doi.org/10.1103/PhysRevD.93.084024)
- Keitel, D., & Ashton, G. 2018, *Class. Quant. Grav.*, 35, 205003, doi: [10.1088/1361-6382/aade34](https://doi.org/10.1088/1361-6382/aade34)
- Keitel, D., Prix, R., Papa, M. A., Leaci, P., & Siddiqi, M. 2014, *Phys. Rev.*, D89, 064023, doi: [10.1103/PhysRevD.89.064023](https://doi.org/10.1103/PhysRevD.89.064023)
- Kokkotas, K. D., & Schwenzer, K. 2016, *Eur. Phys. J.*, A52, 38, doi: [10.1140/epja/i2016-16038-9](https://doi.org/10.1140/epja/i2016-16038-9)
- LIGO. 2018a, The O1 Data Release, <https://www.gw-openscience.org/O1/>
- . 2018b, The O2 Data Release, <https://www.gw-openscience.org/O2/>
- . 2018c, O2 Summary, https://www.gw-openscience.org/summary_pages/detector_status/O2/
- . 2018d, LIGO Open Science Center, <https://www.gw-openscience.org/>
- Lindblom, L., Owen, B. J., & Morsink, S. M. 1998, *Phys. Rev. Lett.*, 80, 4843, doi: [10.1103/PhysRevLett.80.4843](https://doi.org/10.1103/PhysRevLett.80.4843)
- Marshall, F. E., Gotthelf, E. V., Zhang, W., Middleditch, J., & Wang, Q. D. 1998, *Astrophys. J.*, 499, L179, doi: [10.1086/311381](https://doi.org/10.1086/311381)
- NICER. 2017, The Neutron Star Interior Composition Explorer Mission, <https://heasarc.gsfc.nasa.gov/docs/nicer/>
- Owen, B. J. 2010, *Phys. Rev.*, D82, 104002, doi: [10.1103/PhysRevD.82.104002](https://doi.org/10.1103/PhysRevD.82.104002)
- Owen, B. J., Lindblom, L., Cutler, C., et al. 1998, *Phys. Rev.*, D58, 084020, doi: [10.1103/PhysRevD.58.084020](https://doi.org/10.1103/PhysRevD.58.084020)
- Ozel, F., Psaltis, D., Guver, T., et al. 2016a, *Astrophys. J.*, 820, 28, doi: [10.3847/0004-637X/820/1/28](https://doi.org/10.3847/0004-637X/820/1/28)
- . 2016b, Neutron Stars Tabulated Equations of State, <http://xtreme.as.arizona.edu/NeutronStars/>
- Paschalidis, V., & Stergioulas, N. 2017, *Living Rev. Rel.*, 20, 7, doi: [10.1007/s41114-017-0008-x](https://doi.org/10.1007/s41114-017-0008-x)
- Python. 2019, Curve Fitting documentation, <https://docs.scipy.org/doc/scipy/reference/optimize.html#curve-fitting>
- Steltner, B., Papa, M., Eggenstein, H.-B., et al. 2020
- Townsley, L. K., Broos, P. S., Feigelson, E. D., Garmire, G. P., & Getman, K. V. 2006, *The Astronomical Journal*, 131, 2164, doi: [10.1086/500535](https://doi.org/10.1086/500535)
- Vallisneri, M., Kanner, J., Williams, R., Weinstein, A., & Stephens, B. 2015, *Journal of Physics: Conference Series*, 610, 012021, doi: [10.1088/1742-6596/610/1/012021](https://doi.org/10.1088/1742-6596/610/1/012021)

APPENDIX

A. EXCLUDED FREQUENCY BANDS

The tables in this appendix contain the complete list of frequency bands excluded from the analysis and from the upper limit results.

Table A1. Excluded frequency bands in the O1 search run

Hanford (LHO)			Livingston (LLO)		
central f	$-\Delta f$	$+\Delta f$	central f	$-\Delta f$	$+\Delta f$
[Hz]	[Hz]	[Hz]	[Hz]	[Hz]	[Hz]
86.000000	0.004856	0.004360	86.749750	0.004861	0.004371
86.500000	0.004856	0.004360	87.749725	0.004861	0.004371
87.000000	0.004856	0.004360	87.900000	0.004361	0.003871
87.500000	0.004856	0.004360	88.400000	0.004361	0.003871
88.000000	0.004356	0.003860	88.749700	0.004861	0.004371
88.000000	0.004856	0.004360	89.749675	0.004861	0.004371
88.500000	0.004856	0.004360	90.300000	0.004361	0.003871
89.000000	0.004856	0.004360	90.749650	0.004861	0.004371
89.500000	0.004856	0.004360	90.800000	0.004361	0.003871
90.000000	0.004856	0.004360	91.300000	0.004361	0.003871
90.500000	0.004856	0.004360	91.749625	0.004861	0.004371
91.000000	0.004856	0.004360	92.749600	0.004861	0.004371
91.500000	0.004856	0.004360	93.700000	0.004361	0.003871
92.000000	0.004856	0.004360	93.749575	0.004861	0.004371
92.500000	0.004856	0.004360	94.200000	0.004361	0.003871
93.000000	0.004856	0.004360	94.749550	0.004861	0.004371
93.500000	0.004856	0.004360	95.749525	0.004861	0.004371
94.000000	0.004856	0.004360	95.883160	0.010261	0.006571
94.238100	0.006856	0.006360	96.600000	0.004361	0.003871
94.244700	0.006856	0.006360	96.749500	0.004861	0.004371
94.500000	0.004856	0.004360	97.100000	0.004361	0.003871
95.000000	0.004856	0.004360			
95.500000	0.004856	0.004360			
96.000000	0.004356	0.003860			
96.000000	0.004856	0.004360			
96.500000	0.004856	0.004360			
97.000000	0.004856	0.004360			

Table A2. Excluded frequency bands in the O2.1 and O2.2 search runs

Hanford (LHO)					Livingston (LLO)				
central f	$-\Delta f$	$+\Delta f$	$-\Delta f$	$+\Delta f$	central f	$-\Delta f$	$+\Delta f$	$-\Delta f$	$+\Delta f$
[Hz]	[Hz]	[Hz]	[Hz]	[Hz]	[Hz]	[Hz]	[Hz]	[Hz]	[Hz]
85.998700	0.001781	0.001974	0.002815	0.002971	91.998700	0.001781	0.001974	0.002815	0.002971
86.000000	0.001781	0.001974	0.002815	0.002971	92.000000	0.001781	0.001974	0.002815	0.002971
86.500000	0.003641	0.003834	0.004675	0.004831	92.500000	0.003641	0.003834	0.004675	0.004831
86.749837	0.001781	0.001974	0.002815	0.002971	92.749745	0.001781	0.001974	0.002815	0.002971
86.998700	0.001781	0.001974	0.002815	0.002971	92.998700	0.001781	0.001974	0.002815	0.002971
87.000000	0.001781	0.001974	0.002815	0.002971	93.000000	0.001781	0.001974	0.002815	0.002971
87.500000	0.003641	0.003834	0.004675	0.004831	93.500000	0.003641	0.003834	0.004675	0.004831
87.749822	0.001781	0.001974	0.002815	0.002971	93.749729	0.001781	0.001974	0.002815	0.002971
87.998700	0.001781	0.001974	0.002815	0.002971	93.998700	0.001781	0.001974	0.002815	0.002971
88.000000	0.001781	0.001974	0.002815	0.002971	94.000000	0.001781	0.001974	0.002815	0.002971
88.500000	0.003641	0.003834	0.004675	0.004831	94.500000	0.003641	0.003834	0.004675	0.004831
88.749806	0.001781	0.001974	0.002815	0.002971	94.749714	0.001781	0.001974	0.002815	0.002971
88.889400	0.001781	0.001974	0.002815	0.002971	94.998700	0.001781	0.001974	0.002815	0.002971
88.889840	0.001781	0.001974	0.002815	0.002971	95.000000	0.001781	0.001974	0.002815	0.002971
88.998700	0.001781	0.001974	0.002815	0.002971	95.500000	0.003641	0.003834	0.004675	0.004831
89.000000	0.001781	0.001974	0.002815	0.002971	95.749698	0.001781	0.001974	0.002815	0.002971
89.500000	0.003641	0.003834	0.004675	0.004831	95.998700	0.001781	0.001974	0.002815	0.002971
89.749791	0.001781	0.001974	0.002815	0.002971	96.000000	0.001781	0.001974	0.002815	0.002971
89.998700	0.001781	0.001974	0.002815	0.002971	96.500000	0.003641	0.003834	0.004675	0.004831
90.000000	0.001781	0.001974	0.002815	0.002971	96.749683	0.001781	0.001974	0.002815	0.002971
90.500000	0.003641	0.003834	0.004675	0.004831	96.998700	0.001781	0.001974	0.002815	0.002971
90.749775	0.001781	0.001974	0.002815	0.002971					
90.998700	0.001781	0.001974	0.002815	0.002971					
91.000000	0.001781	0.001974	0.002815	0.002971					
91.160252	0.005621	0.005814	0.006655	0.006811					
91.500000	0.003641	0.003834	0.004675	0.004831					
91.749760	0.001781	0.001974	0.002815	0.002971					

B. UPPER LIMITS ON THE GRAVITATIONAL WAVE AND THE SATURATION AMPLITUDE

Table B1 shows that there are upper limits in every 0.5 Hz band. The central frequency f of each band is indicated in the first column. We stress again that the $h_0^{90\%}$ and $\alpha^{90\%}$ upper limits do not hold for the subbands of Appendix A.

Table B1. Upper Limits on the Gravitational-wave and Saturation Amplitudes

Spin-down limit			O1				O2.1				O2.2			
f	$h_0^{\text{sd}}_{\text{min}}$	$h_0^{\text{sd}}_{\text{max}}$	$h_0^{90\%}$	$\alpha^{90\%}$	$\sqrt{S_h}$	$\mathcal{D}^{90\%}$	$h_0^{90\%}$	$\alpha^{90\%}$	$\sqrt{S_h}$	$\mathcal{D}^{90\%}$	$h_0^{90\%}$	$\alpha^{90\%}$	$\sqrt{S_h}$	$\mathcal{D}^{90\%}$
[Hz]	$[10^{-26}]$	$[10^{-26}]$	$[10^{-25}]$		$\left[\frac{10^{-23}}{\sqrt{\text{Hz}}}\right]$	$\left[\frac{1}{\sqrt{\text{Hz}}}\right]$	$[10^{-25}]$		$\left[\frac{10^{-23}}{\sqrt{\text{Hz}}}\right]$	$\left[\frac{1}{\sqrt{\text{Hz}}}\right]$	$[10^{-25}]$		$\left[\frac{10^{-23}}{\sqrt{\text{Hz}}}\right]$	$\left[\frac{1}{\sqrt{\text{Hz}}}\right]$
86.0	1.39	2.27	$1.22^{+0.080}_{-0.077}$	0.26	1.01	83.1	$1.22^{+0.081}_{-0.078}$	0.26	0.87	71.5	$1.09^{+0.070}_{-0.070}$	0.23	0.82	75.4
86.5	1.23	2.42	$1.16^{+0.072}_{-0.071}$	0.24	1.04	89.7	$1.21^{+0.077}_{-0.075}$	0.26	0.86	71.2	$1.11^{+0.070}_{-0.071}$	0.23	0.82	73.9
87.0	1.10	2.60	$1.24^{+0.079}_{-0.077}$	0.26	1.10	88.4	$1.21^{+0.077}_{-0.075}$	0.25	0.86	70.7	$1.09^{+0.068}_{-0.068}$	0.23	0.82	75.5
87.5	1.01	2.76	$1.16^{+0.072}_{-0.071}$	0.24	1.07	92.2	$1.26^{+0.083}_{-0.080}$	0.26	0.86	68.5	$1.11^{+0.070}_{-0.070}$	0.23	0.83	74.9
88.0	0.95	2.92	$1.14^{+0.069}_{-0.069}$	0.23	1.01	88.7	$1.20^{+0.074}_{-0.073}$	0.24	0.86	71.5	$1.12^{+0.070}_{-0.070}$	0.23	0.84	74.6
88.5	0.89	3.05	$1.13^{+0.071}_{-0.070}$	0.22	0.99	87.2	$1.25^{+0.085}_{-0.081}$	0.25	0.85	68.2	$1.13^{+0.071}_{-0.070}$	0.22	0.83	73.2
89.0	0.94	3.17	$1.13^{+0.070}_{-0.070}$	0.22	0.97	85.8	$1.23^{+0.080}_{-0.078}$	0.24	0.85	69.2	$1.10^{+0.070}_{-0.070}$	0.21	0.83	75.2
89.5	0.99	3.27	$1.59^{+0.081}_{-0.081}$	0.30	0.99	62.0	$1.23^{+0.079}_{-0.076}$	0.23	0.86	70.0	$1.07^{+0.067}_{-0.068}$	0.20	0.83	77.3
90.0	1.04	3.36	$1.15^{+0.069}_{-0.068}$	0.22	0.96	83.3	$1.20^{+0.074}_{-0.073}$	0.23	0.85	71.1	$1.09^{+0.072}_{-0.072}$	0.20	0.83	75.9
90.5	1.08	3.43	$1.12^{+0.069}_{-0.068}$	0.21	0.95	84.7	$1.19^{+0.076}_{-0.074}$	0.22	0.85	71.1	$1.12^{+0.071}_{-0.071}$	0.21	0.82	73.3
91.0	1.11	3.49	$1.15^{+0.071}_{-0.070}$	0.21	0.95	82.9	$1.20^{+0.078}_{-0.076}$	0.22	0.85	71.1	$1.09^{+0.069}_{-0.070}$	0.20	0.82	75.4
91.5	1.14	3.54	$1.15^{+0.070}_{-0.069}$	0.20	0.96	83.2	$1.20^{+0.079}_{-0.076}$	0.21	0.86	71.9	$1.08^{+0.071}_{-0.071}$	0.19	0.83	76.9
92.0	1.16	3.57	$1.12^{+0.069}_{-0.069}$	0.20	0.95	85.0	$1.26^{+0.083}_{-0.080}$	0.22	0.86	68.3	$1.16^{+0.071}_{-0.071}$	0.20	0.83	71.3
92.5	1.17	3.61	$1.10^{+0.070}_{-0.070}$	0.19	0.94	85.9	$1.24^{+0.082}_{-0.079}$	0.21	0.85	68.9	$1.05^{+0.071}_{-0.077}$	0.18	0.82	78.2
93.0	1.18	3.63	$1.08^{+0.068}_{-0.068}$	0.18	0.93	86.2	$1.20^{+0.075}_{-0.073}$	0.20	0.85	70.8	$1.13^{+0.071}_{-0.071}$	0.19	0.82	72.9
93.5	1.17	3.64	$1.06^{+0.067}_{-0.069}$	0.18	0.92	87.0	$1.22^{+0.082}_{-0.079}$	0.20	0.85	69.5	$1.19^{+0.076}_{-0.075}$	0.20	0.86	72.0
94.0	1.22	3.65	$1.07^{+0.069}_{-0.069}$	0.18	0.91	85.4	$1.31^{+0.083}_{-0.081}$	0.22	0.84	64.1	$1.14^{+0.072}_{-0.071}$	0.19	0.85	74.6
94.5	1.22	3.65	$1.06^{+0.067}_{-0.069}$	0.17	0.90	85.2	$1.22^{+0.081}_{-0.078}$	0.20	0.83	67.9	$1.06^{+0.068}_{-0.071}$	0.17	0.80	75.9
95.0	1.21	3.65	$1.05^{+0.068}_{-0.067}$	0.17	0.89	85.1	$1.16^{+0.072}_{-0.072}$	0.18	0.82	70.3	$1.09^{+0.069}_{-0.070}$	0.17	0.79	72.2
95.5	1.19	3.66	$1.05^{+0.068}_{-0.070}$	0.17	0.89	84.3	$1.14^{+0.072}_{-0.071}$	0.18	0.81	70.8	$1.00^{+0.066}_{-0.068}$	0.16	0.78	77.9
96.0	1.30	3.66	$1.10^{+0.069}_{-0.069}$	0.17	0.88	79.8	$1.16^{+0.075}_{-0.074}$	0.18	0.80	69.1	$0.99^{+0.068}_{-0.072}$	0.15	0.77	78.3
96.5	1.56	2.92	$1.01^{+0.065}_{-0.066}$	0.15	0.87	86.5	$1.09^{+0.068}_{-0.069}$	0.17	0.80	73.2	$1.03^{+0.065}_{-0.066}$	0.16	0.77	75.0
97.0	1.56	2.90	$1.02^{+0.064}_{-0.064}$	0.15	0.87	85.5	$1.18^{+0.076}_{-0.075}$	0.18	0.80	67.5	$1.00^{+0.065}_{-0.067}$	0.15	0.77	77.5